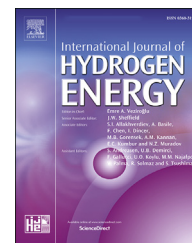




ELSEVIER

Available online at [www.sciencedirect.com](http://www.sciencedirect.com)

ScienceDirect

journal homepage: [www.elsevier.com/locate/he](http://www.elsevier.com/locate/he)

# Model predictive control of an on-site green hydrogen production and refuelling station

P. Cardona<sup>a,\*</sup>, R. Costa-Castelló<sup>b</sup>, V. Roda<sup>d</sup>, J. Carroquino<sup>d,e</sup>, L. Valiño<sup>c</sup>, M. Serra<sup>a</sup>

<sup>a</sup> Institut de Robòtica i Informàtica Industrial, CSIC-UPC, Llorens I Artigas 4-6, Barcelona, 08028, Spain

<sup>b</sup> Universitat Politècnica de Catalunya (UPC), Carrer de Jordi Girona, 31, Barcelona, 08034, Spain

<sup>c</sup> Instituto de Carboquímica (Consejo Superior de Investigaciones Científicas), C/ de Miguel Luesma Castán, 4, Zaragoza, 50018, Spain

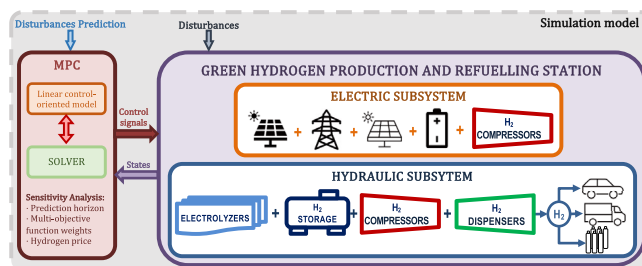
<sup>d</sup> Intergia Energía Sostenible S.L., Maria de Luna 11, Nave 19, Zaragoza, 50018, Spain

<sup>e</sup> Universidad San Jorge, Villanueva de Gállego, Zaragoza, 50830, Spain

## HIGHLIGHTS

- Model Predictive control application for green hydrogen refuelling station.
- Linear modelling of green hydrogen refuelling station.
- Parameter sensitivity analysis of the multi-objective function.
- Prediction horizon sensitivity analysis.
- Model Predictive Control performance advantage compared to rule-based control.

## GRAPHICAL ABSTRACT



## ARTICLE INFO

### Article history:

Received 10 November 2022

Received in revised form

27 December 2022

Accepted 18 January 2023

Available online 14 February 2023

### Keywords:

Hydrogen refuelling station

Model predictive control

Optimization

On-site electrolytic hydrogen

production

## ABSTRACT

The expected increase of hydrogen fuel cell vehicles has motivated the emergence of a significant number of studies on Hydrogen Refuelling Stations (HRS). Some of the main HRS topics are sizing, location, design optimization, and optimal operation. On-site green HRS, where hydrogen is produced locally from green renewable energy sources, have received special attention due to their contribution to decarbonization. This kind of HRS are complex systems whose hydraulic and electric linked topologies include renewable energy sources, electrolyzers, buffer hydrogen tanks, compressors and batteries, among other components. This paper develops a linear model of a real on-site green HRS that is set to be built in Zaragoza, Spain. This plant can produce hydrogen either from solar energy or from the utility grid and is designed for three different types of services: light-duty and heavy-duty fuel cell vehicles and gas containers. In the literature, there is a lack of online control solutions developed for HRS, even more in the form of optimal online control. Hence, for the HRS operation, a Model Predictive Controller (MPC) is designed to solve a weighted

\* Corresponding author.

E-mail address: [pcardona@iri.upc.edu](mailto:pcardona@iri.upc.edu) (P. Cardona).

<https://doi.org/10.1016/j.ijhydene.2023.01.191>

0360-3199/© 2023 The Author(s). Published by Elsevier Ltd on behalf of Hydrogen Energy Publications LLC. This is an open access article under the CC BY-NC-ND license (<http://creativecommons.org/licenses/by-nc-nd/4.0/>).

Solar power  
Green hydrogen production

multi-objective online optimization problem taking into account the plant dynamics and constraints as well as the disturbances prediction. Performance is analysed throughout 210 individual month-long simulations and the effect of the multi-objective weighting, prediction horizon, and hydrogen selling price is discussed. With the simulation results, this work shows the suitability of MPC for HRS control and its significant economic advantage compared to the rule-based control solution. In all simulations, the MPC operation fulfils all required services. Moreover, results show that a seven-day prediction horizon can improve profits by 57% relative to a one-day prediction horizon; that the battery is under-sized; or that the MPC operation strategy is more resolute for low hydrogen selling prices.

© 2023 The Author(s). Published by Elsevier Ltd on behalf of Hydrogen Energy Publications LLC. This is an open access article under the CC BY-NC-ND license (<http://creativecommons.org/licenses/by-nc-nd/4.0/>).

#### Acronyms:

|         |                                       |
|---------|---------------------------------------|
| HRS     | Hydrogen Refuelling Station           |
| MPC     | Model Predictive Control              |
| FCV     | Fuel Cell Vehicles                    |
| HDFV    | Heavy-Duty Fuel cell Vehicle          |
| LDFV    | Light-Duty Fuel cell Vehicle          |
| MEGC    | Multiple Element Gas Container        |
| MG      | Microgrid                             |
| PV      | Photovoltaic                          |
| EMBD_SP | Embedded Solar Panels                 |
| GRD     | Utility Grid                          |
| P&ID    | Piping and Instrumentation Diagram    |
| Ti      | Compressed hydrogen gas tank number i |
| Ci      | Hydrogen compressor number i          |
| Di      | Dispenser number i                    |
| VDS     | Vehicle Demand Signal                 |
| SOC     | State of Charge                       |
| SOM     | Simulation-oriented Model             |
| COM     | Control-oriented Model                |
| BT      | Electrochemical Battery               |
| CS      | Control Signal                        |

## Introduction

Due to the expected increase in hydrogen Fuel Cell Vehicles (FCV) circulation, new Hydrogen Refuelling Stations (HRS) have to be put into operation. Specifically, the International Energy Agency (IEA) [1] states that hydrogen demand for road transport has increased 60% since 2020 to a total of 30 kt annually worldwide in 2021. Moreover, road transport hydrogen demand is expected to increase due to the forecasted increase in FCV from over 59,000 vehicles worldwide in 2022 [1] to 3.3 M vehicles in 2030 [2], and between 100 M and 400 M vehicles by 2050 [2]. This could represent a 0.7 to 8 Mt of hydrogen global demand for road transport according to the Stated Policies Scenario and the Announced Pledges Scenario to Net Zero Emissions, respectively, by 2030 [1].

In Spain, the Ebro Hydrogen Corridor is a clear example of the decisive increasing trend in hydrogen energy and

hydrogen economy's importance. This project plans to achieve 250 kt of renewable hydrogen production with a capacity of 400 MW of renewable generation by 2025, increasing to 1.5 GW of renewable hydrogen production by 2030 [3,4].

In correlation with FCV units and hydrogen production increase, hydrogen delivery infrastructure must improve in availability, performance, and cost. From 700 HRS in operation globally in 2021, 975 HRS were in operation by the end of June 2022, which gives around 60 FCV units per each HRS [1]. In Europe, by 2018, there were about 6.4 FCV units per HRS, which can be compared with 4.8 battery electric vehicles per electric charger [2]. This European ratio of FCV units per HRS is the lowest ratio of all surveyed areas [1]. In Spain, the Ebro Hydrogen Corridor project plans to increase the number of HRS from the actual 6 to 20 by 2025 and 100 by 2030 [3,4].

In spite of the improvements needed, the research done on HRS is rather little, being orders of magnitude lower in the number of published articles than fuel cell or FCV articles, according to Ref. [5].

Different types of HRS have been described in the literature. One first HRS classification criteria refers to hydrogen production location, which gives off-site and on-site HRS.

On-site HRS include the hydrogen production locally at the station. In this type of HRS, different hydrogen production processes can be found, which are mainly steam methane reforming and water electrolysis [2]. Moreover, since the electrical energy consumption of an on-site HRS will be significantly higher than that of an off-site HRS due to hydrogen production and compression, it is crucial to specify the type of HRS electrical energy sources. These energy sources can be renewable energy sources (generally solar or wind) or come from the utility grid. If hydrogen is produced with renewable energy sources, the HRS is called green HRS. If the HRS is able to extract energy from the utility grid, it is called grid-connected HRS and otherwise, stand-alone or self-sustainable HRS. Renewable and utility grid energy sources are not exclusive from each other, which means that HRS can be also grid-connected renewable microgrids, as is the case of study of this work. A grid-connected on-site renewable HRS can bring hydrogen cost lower compared to a stand-alone HRS [2] and improve the demand satisfaction guarantee.

Regarding the HRS target vehicles, HRS dispensing systems are usually designed either to service heavy-duty fuel cell

vehicles at a pressure of 350 barg (35,000 kPa), or light-duty fuel cell vehicles at a of pressure 700 barg (70,000) [2,5].

Moreover, some of the HRS described in the literature integrate fuel cell systems. The fuel cells purpose is to recover electrical energy from the hydrogen in case of need or for performance optimization. This energy may be either injected into the grid, used to feed HRS loads, or used to charge battery electric vehicles. This is especially interesting in stand-alone HRS where electrical energy storage or power may be a constraint.

The first research article on HRS was published in 1982 [6] but more comprehensive models do not appear until 2006 and 2009 [7–9]. The main topics of modelling, sizing, and control are not treated until 2013 when an increase in the published articles is seen. Nevertheless, it is quite recently that the interest in HRS has importantly grown up and more than half of the articles referenced in this work have been published in the 2020–2022 period.

The main topics of on-site HRS studies have been location [10–12], sizing and design optimization [13–18], and control, that will be discussed later.

The HRS configuration and capabilities are very important to differentiate between studies. General HRS subsystems/stages are well-explained in Refs. [2,5]. In the following paragraphs, different articles of the literature are grouped according to their HRS configuration.

Grid-connected HRS layouts are studied in Refs. [14,15,18,19] and stand-alone HRS designs are studied in Refs. [17,20,21].

Green HRS, either grid-connected or stand-alone, can have solar photovoltaic energy source [17,18,21–23] or wind energy source [24]. Both solar photovoltaic and wind energy sources are considered in Refs. [20,25] and diesel generators are considered as a power source in Refs. [13,26].

Water electrolysis is the hydrogen production process considered in all studies except for [27,28], where steam methane reforming and delivered hydrogen are considered, respectively.

Furthermore, some of the works consider an electrochemical battery in the HRS layout [19,27,29].

Another important HRS feature found in several configurations is multi-product capability, meaning the inclusion of electric chargers for battery electric vehicles [13,21,23]. Interestingly, battery-swapping is also modelled in Ref. [29].

Finally, fuel cell stacks are present in HRS layouts studied in Refs. [20,21,30].

Of all the studies referenced in this work, only 4 are based on real HRS plants [9,22,24,31].

Regarding HRS operational control, which is the topic of this work, it has been solved mainly by offline optimal scheduling [14,15,18,23,32–34], where stochasticity, different algorithms or optimal sizing is generally tested.

Offline control methods are those in which the total problem scenario (states and disturbances) is treated at once. This method is usually the result of mathematical optimization or iterative heuristic algorithms. If feasibility in the solution is achieved, the resulting control actions are static, they are scheduled to the stated scenario. This method is exploited by the software HOMER which has been used for techno-

economic analysis in sizing and layout design of HRS [18,25,34].

For any real control problem in which all plant's disturbances can not be perfectly predicted at once prior to starting operation and whose states' dynamics are time-dependent, an online control strategy must be adopted. An online control method will perform in real-time hence its control actions will adapt to the states, disturbances and events as they evolve in a linear time manner. In the energy management field, these methods are usually classic control methods, rule-based control methods or optimal control methods.

Rule-based control strategies are implemented in Refs. [7,20,28,31,35]. More specifically [7], applies a time band schedule, justified by utility grid energy prices, for hydrogen production in which the gas tank is filled just in time at 6 a.m. starting at 9 p.m. of the previous day and, to supply the forecasted demand, hydrogen is also produced to drive the tank to a required level by 5 p.m. starting at 10 a.m. Three rule-based strategies are tested in Ref. [20]. These strategies differ in terms of how renewable energy sources and the fuel cell are utilized to meet the electrolyzer or compressors electric power load. The best results in terms of cost and efficiency are with a strategy that feeds the electric load with renewable energy as much as possible and only uses the fuel cell when renewables are not available. In the case of [31], a variable power threshold strategy is proposed with the intention of maximizing the electrolyzer production in a solar photovoltaic grid-connected HRS. When the threshold in input power is surpassed, green hydrogen is produced and when renewable energy input is under the threshold, power grid energy is consumed. For a solar photovoltaic system sized at 150% of the electrolyzer plant consumption of a grid-connected HRS, this power levelling strategy shows in a small-scale experimental system a 10% increase in electrolyzer utilization without increasing carbon dioxide emissions in hydrogen production compared to a not renewable HRS. In the case of [35], four strategies are proposed, they differ in terms of how the photovoltaic energy input, the utility grid and the electrochemical battery are utilized to meet the demand of charging battery electric vehicles and FCV hydrogen demand. These strategies define different priorities on the fuel cell, electrolyzer, battery and spare hydrogen usage. Attending to Ref. [28], a state machine for the refuelling process is presented. This process decides which of the three-cascaded tanks with different pressure levels is emptied to supply hydrogen demand. This strategy shows a 34% reduction in energy consumption compared to a one-tank storage system.

If the authors are not wrong [24], is the only work found in the literature with a scope similar to the present work, i.e. the online optimal control of an on-site renewable HRS.

Carr .S,et al., [24] develops a nonlinear model of an on-site renewable wind-based grid-connected light-duty vehicle HRS based on a real plant. The HRS consists of one compressor and one storage tank. The model presented is simplified to treat the operational problem at a 30-min sampling time (compressor, electrolyzer, and dispenser electrical consumption are considered to vary synchronously at the sampling time) and the hydrogen demand profile is considered based on an hourly profile. The prediction horizon is fixed at two days. Demand profile scaling effect in performance is analysed as

well as wind turbine sizing and electrolyzer available output range in 30 days-long simulations. Results are analysed in detail based on economical profit.

The main contributions of this article are:

- Presentation of a multi-compressor, multi-storage on-site renewable solar-based and grid-connected HRS based on electrolysis hydrogen production. This plant is set to be built in Zaragoza, Spain. This work presents the first HRS that considers delivering compressed hydrogen directly to the end-user as well as heavy and light-duty vehicle service.
- A linear Simulation-oriented Model (SOM) of the HRS is presented.
- A linear MPC is developed as the online control solution.
- The MPC multi-objective function proposed is defined by three perspectives: profit, regulation and softening.
- MPC performance is thoroughly analysed through 210 simulations.
- The effect of prediction horizon in the MPC performance is analysed.
- Multi-objective weighting effect in the MPC performance is analysed.
- Hydrogen price effect in the MPC performance is analysed.
- The MPC performance will be compared to a rule-based control solution developed by the authors.
- To the authors' knowledge, this is the first study of a multi-storage, multi-compressor HRS controlled by MPC in the literature.

## Case study

This section will present the HRS layout, elements and specifications of the case of study, a real plant that is set to be built in Zaragoza, Spain. With this aim, two diagrams will be introduced and discussed in this section: the hydraulic diagram and the electric diagram.

### Hydraulic diagram

The hydraulic diagram is shown in Fig. 1, which is based on the real P&ID diagram.

In Fig. 1, storage tanks (Ti) are presented as dark blue boxes, compressors (Ci) as red triangles and dispensers (Di) as green

triangles. Blue arrows represent hydrogen paths and as can be seen, there are no bidirectional paths. Since purification and cooling stages are out of the scope of this work, they are not considered. Tanks mass capacities and maximum pressures @ 25°C are resumed in Table 1.

Electrolysis is done by a grid of 22 interconnected electrolyzers, shown as blue rhombus in Fig. 1. Each electrolyzer will consume water and electrical power to produce hydrogen. This power can come from a common grid connection point and/or a direct beam irradiance solar panel (EMBD\_SP) where each electrolyzer unit is embedded. These elements are coupled for efficiency and simplicity reasons based on proprietary technology. The two electrical power sources are shown in Fig. 2.

Next in order in Fig. 1 we find T1, the first and lowest pressure and mass capacity tank of the HRS. This tank's purpose is to be a buffer element between the electrolyzers' output and C1. It is mandatory to have such a tank to unify all the electrolyzers' produced hydrogen as well as to prevent C1 output flow rate fluctuations from damaging any of the electrolyzer units. Its maximum pressure is 2 barg, which is the maximum electrolyzers' output pressure.

In Fig. 1, compressor C1 is responsible for bringing hydrogen pressure from 2 barg to a maximum of 35 barg in T2. The purpose of using multiple tanks in series is to be able to use smaller compressors.

Compressor C2 is responsible for filling the three-tank cascaded subsystem formed by T3<sub>1</sub>, T3<sub>2</sub> and T3<sub>3</sub> at a maximum pressure of 500 barg, as shown in Fig. 1. This subsystem is called cascaded since its purpose is to be filled and emptied in an ordered sequential manner that provides better performance in direct tank-to-tank expansion processes taking advantage of the high pressure of the non-emptied tanks [28]. A 12% reduction in compression energy demand and a 19% less high-pressure hydrogen mass is achieved in the three-tank cascaded system of [36] compared to a one-tank

**Table 1 – Tanks specifications @ 25°C.**

| Tank | Capacity (kg) | P <sub>max</sub> (barg) | P <sub>max</sub> (kPa) |
|------|---------------|-------------------------|------------------------|
| T1   | 11            | 2                       | 200                    |
| T2   | 105           | 35                      | 3500                   |
| T3   | 105           | 500                     | 50,000                 |
| T4   | 15            | 900                     | 90,000                 |

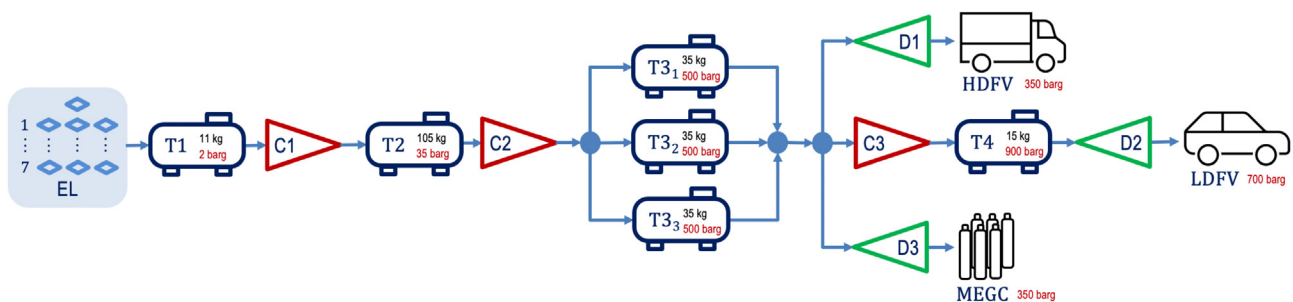


**Fig. 1 – Hydraulic plant diagram.**

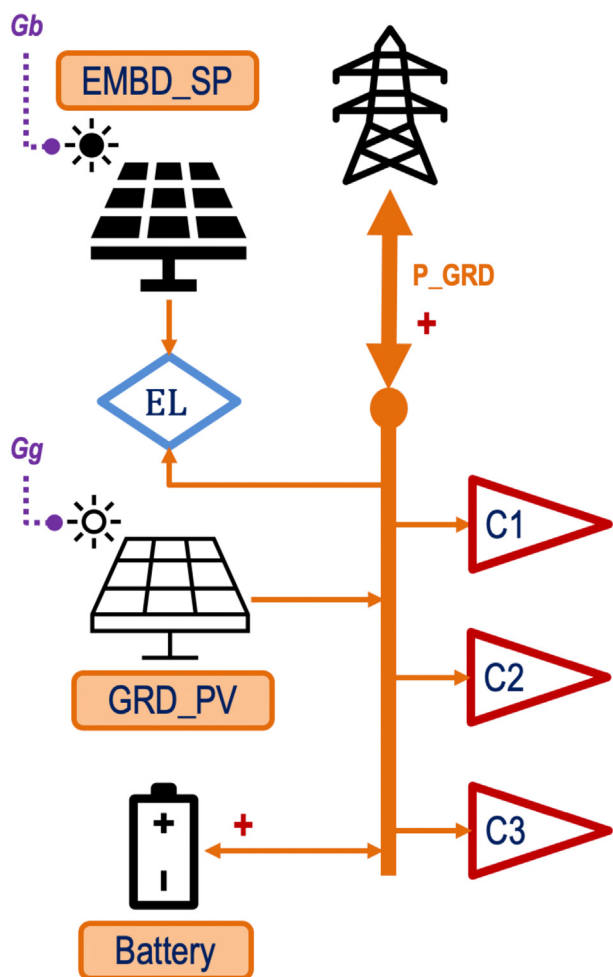


Fig. 2 – Electric plant diagram.

solution. A 6% in energy savings with a three-tank cascaded system in front of a one-tank solution is presented in Ref. [27].

From T3<sub>1</sub>, T3<sub>2</sub> or T3<sub>3</sub> there are three hydrogen paths. In Fig. 1 we see how after the cascaded subsystem we find two dispensers, D1 and D3, and a compressor, C3. Dispensers D1 and D3 are designed to give service at the same maximum pressure level of 350 barg. Nevertheless, they differ in terms of the target client. D1 is designed to refuell Heavy Duty Fuel-cell Vehicles (HDFV) and D3 will fill Multiple Element Gas Containers (MEGC) that will be sold to the end consumer and replaced with empty ones.

Regarding compressor C3 in Fig. 1, it is a necessary component to be able to refuell Light Duty Fuel-cell Vehicles (LDFV) at a target maximum pressure of 700 barg through dispenser D2. In between, T4 is placed as a buffer element that can provide fast tank-to-tank service. Its mass capacity has been set targeting a one full 7 kg LDFV service as buffer capability.

Compressors and dispensers flow ranges @ 25°C are listed in Table 2.

As can be appreciated, multi-stage compression and storage is the approach taken in the HRS layout of this study. This approach provides flexibility which can be used to optimize the process. On the other hand, this approach requires a higher complex control solution.

Table 2 – Compressors and dispensers specifications @ 25°C.

| Element | Maximum Output |                    |
|---------|----------------|--------------------|
|         | kg/h           | Nm <sup>3</sup> /s |
| C1      | 10             | 0.031              |
| C2      | 30             | 0.093              |
| C3      | 2.1            | 0.006              |
| D1      | 432            | 1.335              |
| D2      | 432            | 1.335              |
| D3      | 432            | 1.335              |

### Electric diagram

The case study HRS is grid-connected. Therefore, the system has two types of electrical energy sources, renewable sources and the utility grid. Moreover, the HRS has the capability of storing electrical energy thanks to the electrochemical battery included in the layout.

From a design perspective, the main purpose of the battery is to minimize load peaks in the utility grid. A battery inclusion is interesting since the HRS electrical energy provider will, most certainly, have an upper power constraint depending on the type of contract or location. Costs increase as higher power lines or contracts are required even if the feasibility of a high power connection point at the HRS location is assumed. From a control perspective, an electrical battery brings one more degree of freedom that may contribute to the global optimality of the HRS performance.

The electric system description of the HRS utility grid-connected microgrid (MG) is shown in Fig. 2. It presents all electrolyzers and all compressors as direct active loads. At the electrolyzers block, we can appreciate the two possible sources for hydrogen production discussed before, direct beam irradiance energy and grid energy.

The battery can be independently controlled to supply energy to the MG (discharging) or act as a load (charging), thus being the only MG's active bidirectional element. Battery charging/discharging system has been designed to provide a ± 150 kW range.

Furthermore, the HRS studied integrates a grid-on photovoltaic system (GRD\_PV). GRD\_PV output depends mainly on global irradiance, Gg.

Bidirectional energy paths present positive and negative signs. For those cases, the positive sign is marked in the electric diagram. Denoting the direction that is considered a positive energy transfer.

Fig. 2 presents in purple the disturbances, which are the direct beam irradiance, Gb, and Gg.

In Fig. 2, the power flow to the utility grid (P\_GRD) is bidirectional, hence the HRS can either consume or inject power to the utility grid, buying or selling energy, respectively.

Electrical elements specifications are provided in Table 3.

### Simulation-oriented model

This section will introduce the main assumptions that have been considered to model the plant presented in Section Case

**Table 3 – Electrical elements specifications.**

| Element | Value | Unit                                   |
|---------|-------|--|
| GRD_PV  | 110   | $\frac{\text{kW}}{1000 \text{ W/m}^2}$ |
| Battery | 600   | kWh                                    |
| C1      | 37    | kW                                     |
| C2      | 77    | kW                                     |
| C3      | 11    | kW                                     |

study. Furthermore, the discrete equations that model the HRS dynamics will be given.

### Model assumptions

In order to simplify the HRS model, the next list of assumptions has been made:

- Hydrogen is considered an ideal gas.
- Hydrogen compression and expansion are considered isothermic processes. Hence, hydrogen cooling stages are not considered.
- Hydrogen purity is considered ideal, compressors oil or particles leakage is not considered. Hence, purification stages are not considered.
- Pressure drops along the ducts are neglected.
- Dispensers D1 and D2 output maximum flow rate has been fixed at the value that permits 100% service completion for HDFV and LDFV in one time-step. This value is lower than the real dispenser maximum output (indicated in Table 2).
- Dispenser D3 output maximum flow rate is assumed equal to that of D1.
- Dispenser D1, D2, and D3 have been assumed controllable in a 0–100% range by the control signals  $D1\_CS$ ,  $D2\_CS$  and  $D3\_CS$ , respectively.
- Hydrogen flow rates are independent of tank pressures. Desired compressors' output flow rate has been assumed controllable in a 0–100% range of their specifications shown in Table 2. C1, C2 and C3 will be controlled by control signals  $C1\_CS$ ,  $C2\_CS$  and  $C3\_CS$ , respectively.
- Cascaded  $T3_1$ ,  $T3_2$  and  $T3_3$  subsystem has been assumed as one unique 105 kg, 500 barg tank, addressed as T3.
- Photovoltaic DC-AC inverters, battery bidirectional DC-AC power converter, and ancillary power electronic systems have been considered ideal and they do not add power dynamics or energy losses to the system.
- Battery charging/discharging power has been assumed controllable in a  $\pm 100\%$  range ( $\pm 150$  kW) by  $P\_BT$  control signal.
- Electrolyzers grid-connected and irradiation hydrogen simultaneous production has been considered possible. Total output is assumed upper limited to the value corresponding to  $1200 \text{ W/m}^2$  irradiance-only hydrogen production.
- Electrolyzers grid-connected hydrogen flow rate has been assumed controllable in a 0–100% respective to a 0–6.55 kg/h. Controlled by  $F\_GRD$ .

The electrolyzers' manufacturer provides a linear relationship between the direct beam irradiance,  $G_b$ , and the green hydrogen flow rate output. This irradiance-to-flow relationship factor is  $\beta_{EL\_IR2F}$ . They also provide the electrolyzers' energy consumption data for grid-connected hydrogen flow rate production. This data has been linearized with the  $\alpha_{EL\_F2P}$  flow-to-power factor. Grid-connected hydrogen flow rate output is limited to 6.55 kg/h and controlled by the  $F\_GRD$  signal.

Photovoltaic system GRD\_PV model has been linearized with the  $\beta_{PV\_IR2P}$  factor relating power output with global irradiance input,  $G_g$ .

Compressors' consumption has been linearized, dividing each compressor's nominal power by its nominal output flow rate. As a result,  $\alpha_{C1\_F2P}$ ,  $\alpha_{C2\_F2P}$  and  $\alpha_{C3\_F2P}$  factors are defined for C1, C2 and C3, respectively.

Model linear coefficients are given in Table 4.

Regarding demand modelling, it has been assumed that HDFV, LDFV and MEGC demand are tanks always connected to their respective dispenser. Since HDFV and LDFV services are disturbances to the system, two independent vehicle demand signals,  $VDS\_HDFV$  and  $VDS\_LDFV$ , have been used as disturbances that empty each of the two respective tanks, HDFV and LDFV, to emulate the arrival of the vehicles. These signals will be binary variables (0–1) where 1 indicates that the corresponding vehicle has arrived and needs to be refuelled. For MEGC service, it is implicitly assumed that when the tanks are full, they are replaced with empty ones, hence infinite capacity is implied.

### Model

This subsection will declare the discrete equations that define the dynamics of the 8 states of the Simulation-oriented Model (SOM), in a state-space representation:

$$\mathbf{x}(k+1) = \mathbf{x}(k) + \mathbf{B}\mathbf{u}(k) + \mathbf{B}_d\mathbf{v}(k) \quad (1)$$

with the state vector  $\mathbf{x}(k)$ , controlled variable vector  $\mathbf{u}(k)$  and disturbance vector  $\mathbf{v}(k)$  defined as:

**Table 4 – Linear coefficients.**

| Coefficient        | Value | Unit                                   |
|--------------------|-------|--|
| $\beta_{EL\_IR2F}$ | 10.11 | $\frac{\text{kg/h}}{1000\text{W/m}^2}$ |
| $\beta_{PV\_IR2P}$ | 0.11  | $\frac{\text{kW}}{\text{W/m}^2}$       |
| $\alpha_{EL\_F2P}$ | 60.29 | $\frac{\text{kW}}{\text{kg/h}}$        |
| $\alpha_{C1\_F2P}$ | 3.70  | $\frac{\text{kW}}{\text{kg/h}}$        |
| $\alpha_{C2\_F2P}$ | 2.57  | $\frac{\text{kW}}{\text{kg/h}}$        |
| $\alpha_{C3\_F2P}$ | 5.24  | $\frac{\text{kW}}{\text{kg/h}}$        |

$$\mathbf{x}(k) = \begin{pmatrix} x_1(k) \\ x_2(k) \\ x_3(k) \\ x_4(k) \\ x_{HDFV}(k) \\ x_{LDFV}(k) \\ x_{MEGC}(k) \\ SOC_{BT}(k) \end{pmatrix} \quad \mathbf{u}(k) = \begin{pmatrix} F_{GRD}(k) \\ D1_{CS}(k) \\ D2_{CS}(k) \\ D3_{CS}(k) \\ C1_{CS}(k) \\ C2_{CS}(k) \\ C3_{CS}(k) \\ P_{BT}(k) \end{pmatrix} \quad (2)$$

$$\mathbf{v}(k) = \begin{pmatrix} Gb(k) \\ VDS_{HDFV}(k) \\ VDS_{LDFV}(k) \end{pmatrix}$$

where  $x_i(k)$  states represent the hydrogen mass of each tank at each time-step  $k$ .  $SOC_{BT}$  represents the State of Charge of the battery in %.

Matrix  $\mathbf{B}$  represents the possible hydrogen mass flow paths in Fig. 1 and how they depend on the control inputs  $\mathbf{u}(k)$ :

$$\mathbf{B} = \begin{pmatrix} 6.55 & 0 & 0 & 0 & -10 & 0 & 0 & 0 \\ 0 & 0 & 0 & 0 & 10 & -30 & 0 & 0 \\ 0 & -180 & 0 & -180 & 0 & 30 & 0 & 0 \\ 0 & 0 & -42 & 0 & 0 & 0 & 0 & 0 \\ 0 & 180 & 0 & 0 & 0 & 0 & 0 & 0 \\ 0 & 0 & 42 & 0 & 0 & 0 & 0 & 0 \\ 0 & 0 & 0 & 180 & 0 & 0 & 0 & 0 \\ 0 & 0 & 0 & 0 & 0 & 0 & 0 & \frac{150}{600} \end{pmatrix} \frac{T_s}{3600 \cdot 100} \quad (3)$$

Disturbance vector  $\mathbf{v}(k)$  elements are  $Gb$  in  $Wm^{-2}$  units,  $VDS_{HDFV}(k)$  and  $VDS_{LDFV}(k)$ .

Matrix  $\mathbf{B}_d$  represents the effect of the disturbance vector  $\mathbf{v}(k)$  in each state.  $Gb$  disturbance is considered in  $Wm^{-2}$  units.

$$\mathbf{B}_d = \begin{pmatrix} \frac{\beta_{EL\_IR2P}}{1000} \cdot \frac{T_s}{3600} & & & \\ 0 & 0 & 0 & \\ 0 & 0 & 0 & \\ 0 & -30 & 0 & \\ 0 & 0 & -7 & \\ 0 & 0 & 0 & \\ 0 & 0 & 0 & \end{pmatrix} \quad (4)$$

As can be deduced from  $\mathbf{B}_d$  and  $\mathbf{v}(k)$ , when the vehicle demand signals are 1, there will be a subtraction of 30 kg from the HDFV tank and 7 kg from the LDFV tank. This means that all services considered are from an empty initial state since we can ensure that the tanks are completely full at the new vehicles' arrival, as explained in Section Objective function.

Sampling time,  $T_s$ , has been fixed at 10 min.

The microgrid power balance,  $P_{GRD}(k)$ , will be referenced in the following sections. This balance dictates if energy is being consumed from (positive sign) or injected to (negative sign) the utility grid and is defined in Equation (5).

$$P_{GRD}(k) = \alpha_{EL\_F2P} \cdot \frac{F_{GRD}(k)}{100} \cdot 6.55 \\ + \alpha_{C1\_F2P} \cdot \frac{C1_{CS}(k)}{100} \cdot 11 \\ + \alpha_{C2\_F2P} \cdot \frac{C2_{CS}(k)}{100} \cdot 30 \\ + \alpha_{C3\_F2P} \cdot \frac{C3_{CS}(k)}{100} \cdot 11 \\ + \frac{P_{BT}(k)}{100} \cdot 150 \\ - \beta_{PV\_IR2P} \cdot Gg(k) \quad (5)$$

## MPC formulation

In this section, the Model Predictive Control (MPC) applied to the Simulation-oriented Model (SOM) of the HRS studied will be explained.

An MPC is an interesting control solution for an HRS since they are constrained systems with slow dynamics whose performance can be defined by different perspectives. Therefore, multi-objective functions can be formulated and be highly optimized if state dynamics and disturbances prediction is taken in to account.

For any MPC formulation, a Control-oriented Model (COM), an objective function ( $J$ ) and a set of constraints must be defined. The COM will be internally simulated along an entire defined prediction horizon ( $H_p$ ), starting from measured initial conditions (states and disturbances) of the real plant, in our case, a SOM. At every time-step, a solver will judge a set of control strategies (solver decided control inputs along  $H_p$ ) performance in terms of constraints' violation and the objective function, and it will continue to iterate control strategies until a minimum in the objective function is found without any constraint violation along  $H_p$ . Once this global or local minimum is located, the first control input of the overall strategy that guarantees the minimum will be sent to the real plant, in our case, a SOM. This process is repeatedly executed at each real time-step, but with updated plant and prediction data. Since in MPC practices the prediction data is unveiled at the same rate as the system evolves in real-time and the  $H_p$  is fixed, we refer to  $H_p$  as a rolling prediction horizon.

The number of iterations and thus each optimization elapsed time can be highly influenced by the type of solver, the model complexity and, of course, the  $H_p$  length.

As COM we'll take the same model as the SOM introduced in the last section. This means that the system's dynamics will be perfectly predicted by the MPC. Moreover, the same disturbances will be applied to the COM and the SOM. This means that disturbance uncertainty is not considered.

In the following subsections, the set of constraints and the objective function definition will be assessed.

**Constraints definition**

Constraint declaration is a must in MPC practices. If this type of control has been selected above others, is mostly due to the plant physical states and control inputs constraints.

Following the plant's specifications, the state vector constraints are the ones in Equation (6).

$$\begin{pmatrix} 0 \\ 0 \\ 0 \\ 0 \\ 0 \\ 0 \\ 0 \\ 20 \end{pmatrix} \leq \begin{pmatrix} x_1(k) \\ x_2(k) \\ x_3(k) \\ x_4(k) \\ x_{HDFV}(k) \\ x_{LDFV}(k) \\ x_{MEGC}(k) \\ SOC_{BT}(k) \end{pmatrix} \leq \begin{pmatrix} 11 \\ 105 \\ 105 \\ 15 \\ 30 \\ 7 \\ 5000 \\ 100 \end{pmatrix} \quad (6)$$

The authors have assumed that MEGC are instantly replaced when they are full. For this reason, the constraint defined to  $x_{MEGC}$  in Equation (6) is large enough to emulate this assumption.

Furthermore, control decision variables constraints are listed in Equation (7).

$$\begin{pmatrix} 0 \\ 0 \\ 0 \\ 0 \\ 0 \\ 0 \\ 0 \\ -100 \end{pmatrix} \leq \begin{pmatrix} F\_GRD(k) \\ D1\_CS(k) \\ D2\_CS(k) \\ D3\_CS(k) \\ C1\_CS(k) \\ C2\_CS(k) \\ C3\_CS(k) \\ P\_BT(k) \end{pmatrix} \leq \begin{pmatrix} 100 \\ 100 \\ 100 \\ 100 \\ 100 \\ 100 \\ 100 \\ 100 \end{pmatrix} \quad (7)$$

On the other hand, all disturbances have been left unconstrained.

Finally, the total electrolyzers hydrogen production upper limit assumption is defined in Equation (8).

$$\frac{F\_GRD(k)}{100} \cdot 6.55 + Gb(k) \cdot \frac{\beta_{EL\_IR2F}}{1000} \leq 1200 \cdot \frac{\beta_{EL\_IR2F}}{1000} \quad (8)$$

**Objective function**

In this work, the system's performance has been defined from three different perspectives: economical profit, regulation, and control softening. For this reason, this work presents a multi-objective function. Therefore, scaling and weighting of the independent objectives will be necessary. This section will present the multi-objective function and its scaling.

Let's start with the definition of the profit objective,  $J_P$ , which is the result of the balance between operational cost expenses and energy or hydrogen selling income. Our plant has three types of service, so three income streams would be expected from hydrogen selling, one for each service. Nevertheless, as it will be explained when the regulation objective is addressed, HDFV and LDFV service fulfilment, hence its income, is demanded through the tracking of vehicles' tank setpoints. For this reason, hydrogen selling incomes from HDFV and LDFV services are not considered in  $J_P$ . Energy surplus supplied to the utility grid ( $P\_GRD(k)$  with negative sign) will be assumed to be sold at the same hourly price,  $e_p$ , in €/kWh units, as the energy bought from the grid.  $P\_GRD(k)$  with positive sign will represent the operational MG

expenditure. Finally,  $J_P$  is introduced in Equation (9), where  $H_{2p}$  is the hydrogen selling price in €/kg.

$$J_P(k) = P\_GRD(k) \cdot e_p(k) \cdot \frac{Ts}{3600} - (x_{MEGC}(k) - x_{MEGC}(k-1)) \cdot H_{2p} \quad (9)$$

The regulation objective,  $J_R$ , is defined as the regulation error of  $x_{HDFV}$  and  $x_{LDFV}$  respective to a full mass level, at 30 kg and 7 kg, respectively. The refuelling fulfilment of HDFV or LDFV before the next vehicle's arrival is guaranteed by the MPC operation, otherwise, a constraint violation would appear since when  $VDS\_HDFV$  or  $VDS\_LDFV$  signals are set to 1, 30 and 7 kg are subtracted from the respective vehicles' tanks whose levels are restricted to positive values. Accordingly,  $J_R$  is defined in Equation (10).

$$J_R(k) = (30 - x_{HDFV}(k)) + (7 - x_{LDFV}(k)) \cdot \frac{30}{7} \quad (10)$$

Finally, a softening objective,  $J_S$ , of the control variables is introduced. This is very common in MPC practices. Therefore,  $J_S$  tries to avoid strong variation of control input's values since a switching effect could appear and high and fast actuator variation is, in most cases, a reason for great degradation.  $J_S$  is defined in Equation (11),

$$J_S(k) = (u(k) - u(k-1))^T \cdot Q_{sft\_ind} \cdot (u(k) - u(k-1)) \quad (11)$$

where  $Q_{sft\_ind}$  is a softening weighting matrix. Precisely, it is an 8-element square positive semi-definite diagonal matrix that gives us the freedom to differentiate each control variable softening effect in the overall objective  $J_S$ . Since degradation effects are out of this work's scope, all but dispenser control variables are given the same maximum assumed weight, set at a 1, and 0.5 in case of  $P_{BT}$  since it has double range. Dispenser's control variables ( $D1\_CS$ ,  $D2\_CS$  and  $D3\_CS$ ) weights are set to 0 because dispensers output is wanted as fast as possible when it is feasible, so their actuator variation should not have any penalization. Thus,  $Q_{sft\_ind}$  matrix is defined in Equation (12).

$$Q_{sft\_ind} = \text{diag}(1, 0, 0, 0, 1, 1, 1, 0.5) \quad (12)$$

To be able to address the overall performance result from all three perspectives, one unique objective function  $J_{PRS}$  has been formulated, which is the weighted sum of  $J_P$ ,  $J_R$  and  $J_S$  with  $Q_P$ ,  $Q_R$  and  $Q_S$  as their respective weights. Weighting a multi-objective function is not a trivial task, usually a trial and error process. It is a good practice to first apply normalization between all individual objectives. Normalization allows us to correctly compare objectives and thus better affine their weighting.

In this study, a 0 to 1 static adimensional normalization has been applied, being 0 as the best expected individual objective value. Each normalized objective will be referenced with the added "n" subscript.

Since  $J_P$  can have positive or negative values for economic losses or profits, its  $J_{nP}$  is described as shown in Equation (13).

$$J_{nP}(k) = \frac{J_P(k) - J_{P_{\min}}}{J_{P_{\max}} - J_{P_{\min}}} \quad (13)$$

$J_{P_{\max}}$  is obtained with all involved control inputs in Equation (5) set at 100 and  $Gg$  at 0 as well as  $\Delta x_{MEGC}$ . In the case of  $J_{P_{\min}}$ , all control inputs are set to their minimum value indicated in Equation (7) and  $Gg$  at 1747.9 W/m<sup>2</sup>, which is the maximum hourly global irradiation at Zaragoza, Spain, from a 2005 to 2016 dataset [37]. The maximum  $\Delta x_{MEGC}$  depends on the maximum  $D3\_CS$  value and  $T_s$ , which in our case leads to a 30 kg maximum value. Furthermore,  $e_{P_{\max}}$  is set at 0.48491 €/kWh for both  $J_{P_{\max}}$  and  $J_{P_{\min}}$  factors, being the 2021 maximum in Spain [38]. Finally, these two factors depend on  $H_{2p}$  which in our case will be set at 10 €/kg or 2 €/kg. As a result,  $J_{P_{\max}}$  and  $J_{P_{\min}}$  are defined in Table 5.

$J_{nR}$  scaling is seen in Equation (14).

$$J_{nR}(k) = \frac{J_R(k)}{60} \quad (14)$$

Finally,  $J_{nS}$  is easily scaled as shown in Equation (15).

$$J_{nS}(k) = \frac{J_S(k)}{J_{S_{\max}}} \quad (15)$$

where  $J_{S_{\max}}$  is set at 60,000, which has been obtained solving Equation (11) for a full range  $u$  variation in one time-step.

Therefore, the multi-objective cost function  $J_{PRS}$  is defined in Equation (16).

$$J_{PRS}(k) = J_{nP}(k) \cdot Q_P + J_{nR}(k) \cdot Q_R + J_{nS}(k) \cdot Q_S \quad (16)$$

The total number of time-steps,  $N_p$ , of the  $H_p$  in days unit is defined in Equation (17).

$$N_p = H_p \cdot \frac{86400}{T_s} \quad (17)$$

The control strategy obtained by the MPC is defined in Equation (18) [39].

$$u(k) \triangleq (u(0|k), \dots, u(N_p - 1|k)) \quad (18)$$

$$\min_{u \in \mathbb{R}^{mN_p}} J_{PRS}(x_0, u(k)) \quad (19)$$

MPC open-loop optimization problem is defined in Equation (19) subject to.

- COM defined in Equation (1),
- states constraints over  $N_p$  defined in Equation (6),
- control inputs constraints over  $N_p$  defined in Equation (7),

where the cost function domain is defined as  $J_{PRS}(\bullet) : \mathbb{R}_{\geq 0}^m \times \mathbb{R}_{[-w,w]}^{mN_p} \mapsto \mathbb{R}$  and  $m = 8$  since there are eight states as well as eight control inputs and  $w = 100$ . Moreover,  $x_0$  are

the initial state condition from which the COM evolves. Assuming feasibility in the optimization problem, the first control input set of the optimal control strategy solution,  $u^*(0|k)$ , is applied to the SOM and the process is repeated at the next time instant  $k$ .

## Rule-based control formulation

As is common in control development for energy management problems, the first control solution approach of the authors was to develop a rule-based control. This section presents a rule-based control solution developed for the HRS studied. This formulation is the fruit of the authors' experience. This control solution will be faced as a point of reference to the MPC solution results.

The main advantage of designing and implementing a rule-based control in front of an MPC is simplicity. Moreover, the computational load can be drastically less expensive.

On the other hand, the main disadvantage is that the control actions are not optimal and, to approach the optimal solution a significantly more complex set of rules is necessary.

In our case, the problem has been divided into two independent sections: the day-ahead predictive algorithm and the operational state machine.

### Day-ahead predictive algorithm

The purpose of this algorithm is to schedule the future hours in which the electrolyzers will produce hydrogen with electrical energy from the grid. This scheduling will have a length of 24h and will be updated each day at 00:00 a.m. This means that the only output of the algorithm is the hydrogen flow produced by the electrolyzers with energy from the microgrid,  $F_{GRD}$ , discretized to a sampling time of 1h with a length of 24 values, updated once a day.

The algorithm takes 4 inputs each day at 00:00 a.m.

- The sum of mass of T1, T2, T3 and T4.
- The next 24h of hourly  $G_b$  profile prediction data.
- The next 24h of hourly  $e_p$  profile prediction data.
- The next 24h total HDFV and LDFV hydrogen mass demand prediction.

The main logic of the algorithm is to calculate the next-day deficit of irradiance hydrogen production in terms of the demand, taking into account the state of the plant at the time of calculus. This deficit is calculated through Equations A.1 to A.3 in Appendix section A.

In the case of a positive next-day deficit of hydrogen, its value will be equalled by the equivalent minimum necessary hours of  $F_{GRD}$  at a constant 100% (6.55 kg/h).

The algorithm will choose which are the appropriate hours to maximize  $F_{GRD}$  based on the criteria of choosing first the lowest irradiance and lowest grid energy price hours possible. This criterion is reasonable if the goal is to maximize green hydrogen and minimize economic cost. Moreover, the two principles are normally correlated with night hours being the cheapest energy hours.

**Table 5 –  $J_{P_{\max}}$  and  $J_{P_{\min}}$  values.**

| Factor         | $H_{2p} = 10 \text{ €/kg}$ | $H_{2p} = 2 \text{ €/kg}$ | Unit |
|----------------|----------------------------|---------------------------|------|
| $J_{P_{\max}}$ | 54.16                      | 54.16                     | €    |
| $J_{P_{\min}}$ | -327.66                    | -87.66                    |      |

Since this presents a multi-criteria selection, normalization and weights have been applied, both in a scale of 0–1. Normalization is linearly applied by dividing each hourly  $G_b(k)$  and  $e_p(k)$  prediction of the next 24h by the maximum of the respective profiles in that time band.

Two weights whose sum equals 1 are multiplied independently to each normalized hourly value. One weight multiplies  $G_b(k)$  and the other  $e_p(k)$  normalized prediction of the next 24h each day at 00:00 a.m. Then, the two normalized and weighted vectors are hourly summed up giving as a result a value of 0–1 that values the criteria explained.

Finally, a loop iteratively assigns  $F_{GRD}$  at its maximum value as many hours as necessary to cover a positive next-day deficit of hydrogen, choosing from the lowest to the highest normalized and weighted hour.

This algorithm's prediction horizon has been set at a one-day length to facilitate demand satisfaction since  $F_{GRD}$  will cover the daily demand deficit. A longer prediction horizon heuristic algorithm could be developed. Nevertheless, a more complex multi-criteria in the scheduling should be applied. The current criteria would be potentially less robust as the length of the prediction horizon is increased. This is because the current scheduling criteria could potentially result in  $F_{GRD}$  scheduled to be activated at the end of the prediction horizon if the lowest energy price and irradiance are found during that time band. As the prediction horizon increases, this potential effect could bring the system to not be able to supply the early demand events.

### Operational state machine

A finite-state machine has been developed to control dispensers, compressors, and the charging/discharging task of the battery. Hence, the state machine controls all inputs described in Equation (7) except for  $F_{GRD}$ . As inputs, all states and  $F_{GRD}$  are necessary.

Dispensers ( $D1_{CS}$  and  $D2_{CS}$ ) are set to 100% for one time-step whenever  $VDS_{HDFV}(k)$  or  $VDS_{LDFV}(k)$  are 1, respectively.

The MEGC dispenser ( $D3_{CS}$ ) will be set to a 25% when T3 mass is greater than 70 kg and T4 mass is greater than 7 kg. It will be put back to 0% when T3 mass is lower than 60 kg (two HDFV services) or T4 is less than 7 kg (one LDFV service).

Compressor are enabled whenever  $C1_{CS}$ ,  $C2_{CS}$  or  $C3_{CS}$  are greater than 0. This will happen when the respective input tank hydrogen mass is higher than a minimum level and the respective output tank hydrogen mass is lower than its maximum. Each respective signal will be 0 whenever one of the two mentioned conditions are not met.

When compressors are enabled, their control signal will be defined by a function developed. This function takes a relative state of the input tank mass and output tank mass in terms of the maximum negative increment of both tanks in one time-step. This function has been designed to fill the respective output tank as much as possible, it is defined in Equation B.1 of Appendix Section B.

In the case of C1, three states are proposed, two are the same as C2 and C3 and the last state depends on  $F_{GRD}$ . This is justified by trial and error because when  $F_{GRD}$  is put to 100%

by the day-ahead predictive algorithm, higher C1 flow is required if T1 is a near-full state.

Finally, the control logic applied to  $P_{BT}$  is to charge the battery whenever a surplus of energy happens and the battery is not fully charged, limited to 150 kW charge power. The battery will be discharged if  $SOC_{BT}$  is greater than 20% at the excess of electric load respective to a 100 kW threshold, limited to –150 kW of discharging power.

The operational state machine diagram is presented in Figure B1 of Appendix Section B.

### Simulation setup

This work analyses the MPC performance as a control solution for the operation of the proposed HRS and its dependency on  $H_p$ , the multi-objective weighting configuration, and  $H_{2p}$ . For this reason, 210 simulations have been executed using SOM along which  $H_p$ ,  $Q_p$ ,  $Q_R$ ,  $Q_S$  and  $H_{2p}$  are iterated all together in the following manner.

- $H_p$  has been iterated from 1 to 7 days of prediction data length.
- Hydrogen selling price,  $H_{2p}$ , has been iterated over a 2 €/kg and 10 €/kg value.
- $Q_p$  and  $Q_R$  values have been iterated over a 10, 20, 40, 60 and 80% value.
- $Q_S$  has been left to the possible set of values that the sum of all three weights under a 100% value leads to. That solves for an iteration over a 10, 20, 40, 50, 70, and 80% value.

Then, 2 simulations with the rule-based control applied to the SOM have been executed. One with  $H_{2p}$  set at 2 €/kg and the other with  $H_{2p}$  set at 10 €/kg. This two 10 €/kg. This two simulations will function as a point of reference for any MPC results.

All simulations have been done with the same set of conditions.

- Hourly direct and global irradiance  $G_b$  and  $G_g$  time series from January 2016 in Zaragoza, Spain [37].  $G_b$  profile is shown in Fig. 11.
- Hourly energy price  $e_p$  time series from January 2021 in Spain [38]. The profile is shown in Fig. 11.
- $VDS_{HDFV}(k)$  signal value equal to one every 12h starting at 8 a.m.
- $VDS_{LDFV}(k)$  signal value equal to one once a day at 14 p.m.
- Simulation length: 31 days.
- Prediction data length: 31 days +  $H_p$ [days].
- Simulation disturbance profiles are assumed equal to the predicted disturbance profiles introduced to the MPC or the day-ahead predictive algorithm.
- All states' initial conditions are set at their maximum value except for  $x_{MEGC}$  that starts from an empty state.

As can be appreciated, target HDFV and LDFV service is set at a total of 67 kg/day, corresponding to two 30 kg HDFV and one 7 kg LDFV per day.

January has been selected since Spain's winter performance is expected to be lower.

In the case of the rule-based control, the day-ahead predictive algorithm will take a 40% of the maximum 235 kg of hydrogen that the HRS can store as the minimum threshold hydrogen mass that the HRS should store at the moment of calculus, referenced as  $\lambda$  in Equation A.3 of the Appendix Section A. Moreover, the day-ahead predictive algorithm has weighted low-irradiance hours with a 0.8 value.

Simulation has been done with Matlab®, MPC formulation developed using Yalmip [40] environment with Gurobi [41] as the selected solver. The rule-based solution has been developed using Simulink and the Stateflow toolbox. The PC main specs are an Intel® Core™ i7-10700 CPU and 32 GB of RAM.

## Results and discussion

This section will present the most important results obtained from the simulations. Figs. 3–8 analysis corresponds to  $H_p$  set at 2 €/kg. Figs. 9 and 10 will discuss the effect of  $H_p$  variation.

Firstly, the question that arises is how  $H_p$  and weighting affect the HRS states. For all  $H_p$  settings, the averaged effect analysis can be extracted from Figs. 3–5.

In Fig. 3, we can see how  $H_p$  affects the 31 days of simulation average value of the states. For  $x_1$ ,  $x_2$ ,  $x_3$  and  $x_4$  we see that the average mass generally increases along with  $H_p$  for all weighting configurations. This difference is reduced as  $H_p$  increases, denoting a convergence value for long  $H_p$  settings. There appears that a profit-seeking objective (high  $Q_p$ ) results in a higher mass average in states  $x_1$  and  $x_2$ . On the contrary,  $x_4$  decreases with a high  $Q_p$ .

In Fig. 4 we can appreciate how demand has been serviced from the  $x_{HDFV}$  and  $x_{LDFV}$  behaviour. Having a practically constant average at the upper limit of 30 kg and 7 kg, respectively, means that all services have been completed in one sample time. When we appreciate values under the upper

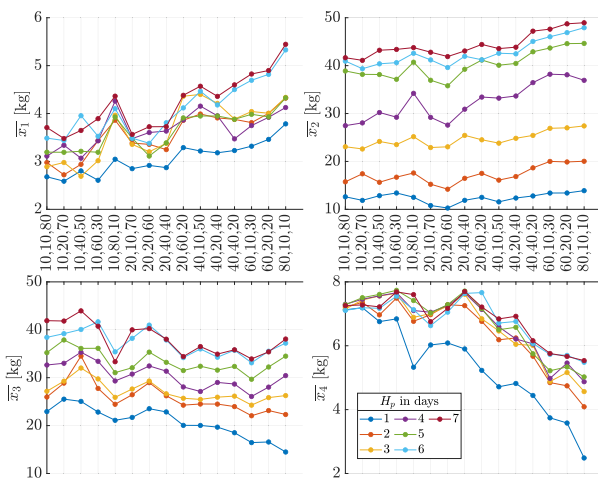


**Fig. 3** – Average simulation state value ( $x_1$ ,  $x_2$ ,  $x_3$  and  $x_4$ ) in terms of  $H_p$  and weight configuration as x-axis, in  $Q_p, Q_R, Q_S$  [%] format,  $H_{2p} = 2$  €/kg.

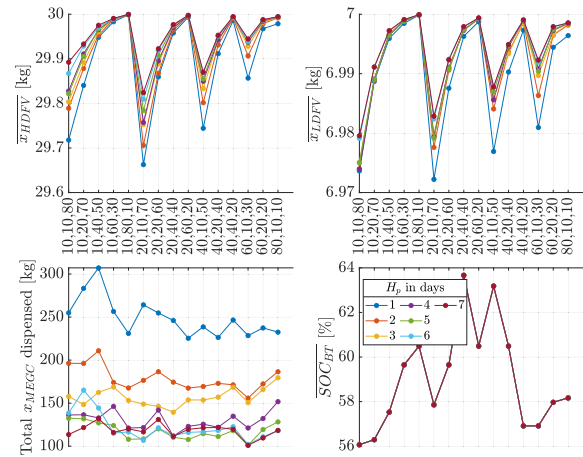


**Fig. 4** – Average simulation state value ( $x_{HDFV}$ ,  $x_{LDFV}$ ,  $x_{MEGC}$  and  $SOC_{BT}$ ) in terms of  $H_p$  and weight configuration as x-axis, in  $Q_p, Q_R, Q_S$  [%] format,  $H_{2p} = 2$  €/kg.

limits means that in some cases refuelling completion has been acquired in more than 10 min. We can see low weighted  $Q_R$  cases, in both tanks, where this happens. It is also true that the difference is insignificant which leads us to the conclusion that  $Q_R$  has been weighted highly enough to achieve complete service fulfilment in one time-step.

In Fig. 4, the total  $x_{MEGC}$  dispensed decreases with longer  $H_p$ . Again, the effect is reduced while  $H_p$  acquires high values, bringing the average to a relative convergence value. In most  $H_p$  sets it is particularly interesting how the most profit-seeking weighting configuration results in slightly less hydrogen mass sold to MEGC, this seems contradictory since it is a direct sell. This could be explained since a longer prediction unveils more critical situations to be overcome so a more

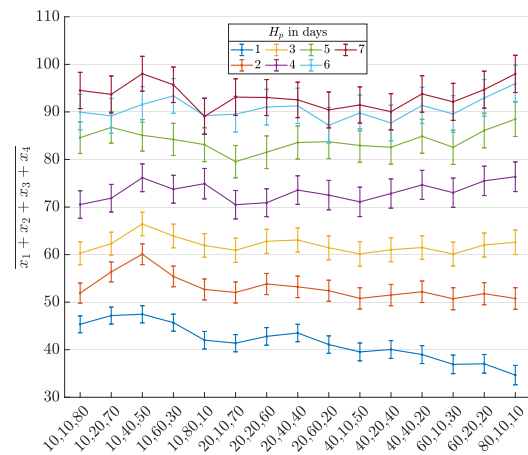


**Fig. 5** – Average simulation HRS mass ( $x_1 + x_2 + x_3 + x_4$ ) in terms of  $H_p$  and weight configuration as x-axis, in  $Q_p, Q_R, Q_S$  [%] format,  $H_{2p} = 2$  €/kg.

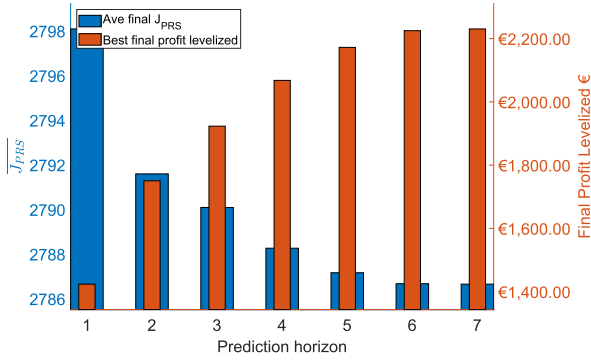


**Fig. 6** – All weighting configuration average of the final  $J_{PRS}$  value and best final leveled profit in terms of  $H_p$  as x-axis,  $H_{2p} = 2 \text{ €/kg}$ .

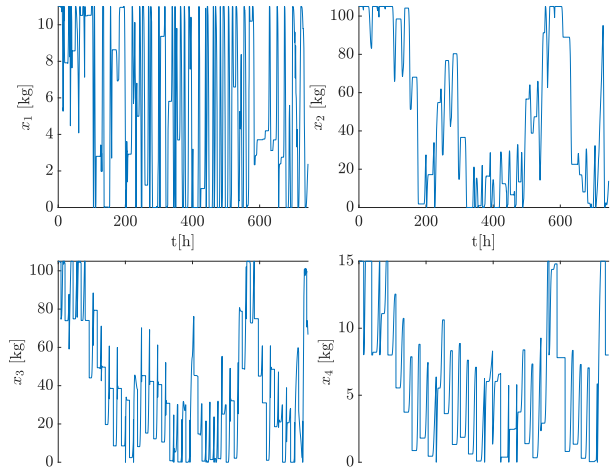


**Fig. 8** –  $x_1, x_2, x_3$  and  $x_4$  evolution along the month of simulation with  $H_p$  set at seven days and 80,10,10[%] weight configuration, x-axis in hour time units,  $H_{2p} = 2 \text{ €/kg}$ .

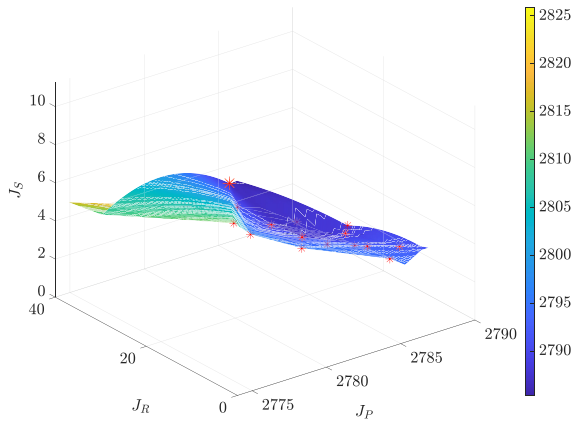


**Fig. 7** –  $J_P, J_R$  and  $J_S$  graphic for  $H_p$  set at seven days,  $H_{2p} = 2 \text{ €/kg}$ .

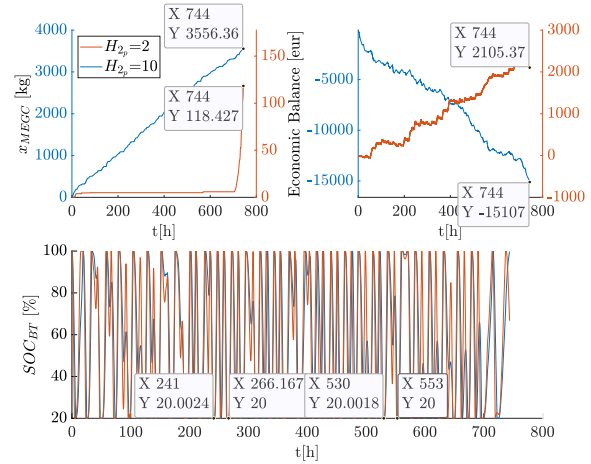


**Fig. 9** –  $x_{MEGC}$ , Economic balance and  $SOC_{BT}$  evolution along the month of simulation with  $H_p$  set at seven days and 80,10,10[%] weight configuration, x-axis in hour time units,  $H_{2p} = 2 \text{ €/kg}$  and  $H_{2p} = 10 \text{ €/kg}$ .

conservative hydrogen selling control strategy should be taken if a longer prediction is available, which is the case. This result is very interesting because it shows that the optimal hydrogen mass to be dispensed to MEGC is around 100–150 kg of hydrogen.

Finally, an absolute lack of  $H_p$  effect on the  $SOC_{BT}$  state 31-days long average is appreciated in Fig. 4. This could be explained due to the control variable  $P_{BT}$  being capable of discharging/charging the battery in only 3.2 h and its dependency on  $e_p$ , that for all cases it is the same time series. This price profile presents peak and off-peak time bands in the range of hours, as shown in Fig. 11, which are directly responsible for the charging/discharging phase of the battery. This could be the reason why results using longer prediction  $e_p$  data are not affected in short-term decisions (one day at minimum).

In Fig. 5 we can see that the effect of  $H_p$  on the total mass is clearly accentuated and we can appreciate how increasing

this parameter brings the total mass to a certain convergence value. It is also worth mentioning how a profit-seeking objective leads to more mass in the system for high  $H_p$  values.

Moreover, the HRS has remained on average under approximately 42% of its 235 kg of hydrogen capacity. This could be a hint to apply component sizing optimization in further research.

Error bars in Fig. 5 are set with a confidence level of 0.1.

To further understand and analyse the results, a bar graph is presented in Fig. 6. This graph is the performance indicator judged in terms of the multi-objective function defined,  $J_{PRS}$ . This graph also displays which would be the expected leveled profits at the end of the month of simulation.

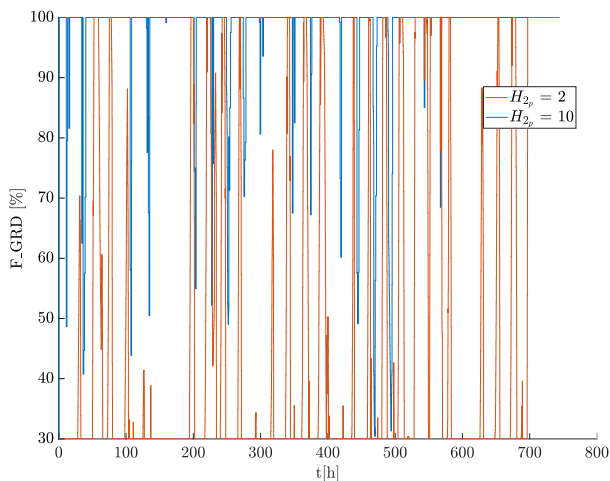


**Fig. 10** –  $F_{GRD}$  evolution along the month of simulation with  $H_p$  set at seven days and 80,10,10[%] weight configuration, x-axis in hour time units,  $H_{2p} = 2 \text{ €/kg}$  and  $H_{2p} = 10 \text{ €/kg}$ .

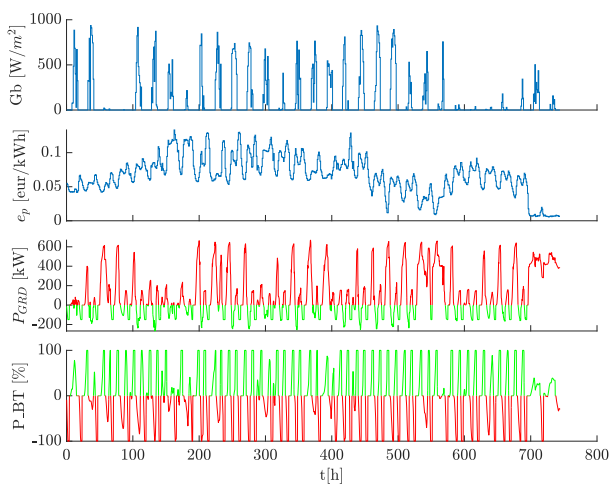


**Fig. 11** –  $G_b$ ,  $e_p$ ,  $P_{GRD}$  and  $P_{BT}$  evolution along the month of simulation with  $H_p$  set at seven days and 80,10,10[%] weight configuration, x-axis in hour time units,  $H_{2p} = 2 \text{ €/kg}$ .

Levelization has been done in order to compare the net profit value of the system considering the mass stored at the system at end of the simulation. Levelized profits have been formulated under the assumption that all mass in tanks 1, 2, 3 and 4 final values would be sold at a  $H_{2p} = 2 \text{ €/kg}$ . Moreover, the 67 kg/day of HDFV and LDFV services have been all acquainted as profits at a  $H_{2p} = 2 \text{ €/kg}$ .

From Fig. 6, we can note that longer  $H_p$  have permitted the solver to find better optimal solutions, for all weighting configurations, since lower  $J_{PRS}$  and higher profits are acquired as a result of increasing  $H_p$ . As explained, lower  $J_{PRS}$  mean higher profits at the end of the month. There exists an approximately

57% profit increase (800 €) between a one-day or seven-day long  $H_p$ .

From a performance standpoint, a seven-day-long  $H_p$  brings the best results. For this reason, this value has been chosen to analyse how weighting would affect performance and which of the tested configuration would lead to the best overall performance. That analysis is shown in Fig. 7, where the colourmap is related to the  $J_{PRS}$  value and red stars mark the discrete result value for a specific weighting configuration ( $Q_p$ ,  $Q_R$ ,  $Q_S$ ). Linearization between the discrete values has been done to mesh the result. The best weighting configuration corresponds to 80,10,10[%] and it is marked with a bigger red star mark in Fig. 7.

The best configuration being at a weighting configuration of 80,10,10[%] can be somewhat expected since, from all simulations data,  $J_p$  has shown to be the most variant individual objective, as well as almost never being zero. This can be also noted since the  $J_p$  axis of Fig. 7 is orders of magnitude higher than the  $J_R$  or  $J_S$  axis. For this reason, it seems logic that the most significant addend in  $J_{PRS}$  is the higher weighted objective since minimization of  $J_{PRS}$  is the MPC purpose. This realization is an indication that scaling has helped to correctly add meaning to the weighting configuration and their effect.

Finally, Figs. 8–11 show the 31-days long simulation results of the 80,10,10[%] weight configuration for a  $H_p$  set at seven days.

Fig. 8 shows  $x_1$ ,  $x_2$ ,  $x_3$  and  $x_4$  evolution. It can be noted how  $x_4$  seems to present a pattern in which it is filled just before an LDFV arrival, an event that rapidly brings down the state's value, as expected. It is also interesting to note that these four tanks have been completely emptied or filled during short periods of time. In addition,  $x_2$  paced evolution contrasts with the highly variant behaviour of  $x_1$ . A common trend between  $x_2$ ,  $x_3$  and  $x_4$  can be appreciated. They are all at their lowest values from the 200h–500h period, approximately. This could be due to high energy prices, as can be seen in the  $e_p$  time series of Fig. 11.

Fig. 9 compares results obtained with different hydrogen prices. It brings us to the conclusion that hydrogen selling through MEGC has not been profitable for almost all the month-long simulation with  $H_{2p}$  at 2 €/kg.  $x_{MEGC}$  has been stable from the first hours until the time 720h, where the strategy has changed drastically. This is easily relatable to the  $e_p$  increase during that final time period, as shown in shown in Fig. 11. With  $H_{2p}$  at 10 €/kg we see a completely different behaviour from which we can conclude that MEGC service has been profitable all month long almost independently of  $e_p$ .

The Economic Balance shown in Fig. 9 is the result of Equation (9) integration. The data-tips show the final Economic Balance value, which being positive means economical losses and negative means profit. It is important to remember that Equation (9), hence the Economical Balance does not take to account HDFV and LDFV services. These two profit inputs are considered in Fig. 6 for the  $H_{2p}$  at 2 €/kg case, where total positive profits are achieved. As expected the economical result is drastically dependent on  $H_{2p}$ . In the case of  $H_{2p}$  set at 10 €/kg, we see that profits are achieved even accounting only MEGC service.

In addition, sudden positive increments in the Economic Balance of Fig. 9 with  $H_{2p}$  at 2 €/kg can be related to high HRS power consumption periods, as  $P_{GRD}$  shows in Fig. 11.

In Fig. 9 a daily full charge and discharge of the battery can be seen. Data-tips along SOC<sub>BT</sub> evolution show how the optimal solution is to have the battery charging at night and discharging during daylight. This battery behaviour is expected since  $e_p$  is lower at night. Nevertheless, it is surprising to see how this behaviour is almost invariant even with a different  $H_{2p}$  value. This observation in conjunction with the results shown in Fig. 4 brings us to the conclusion that the battery capacity is undersized.

Fig. 10 results, with  $H_{2p}$  at 2 €/kg, mean that grid-connected hydrogen production has been generally not convenient since  $F_{GRD}$  is 0 for long time periods. On the contrary, the result for  $H_{2p}$  at 10 €/kg is expected since the  $x_{MEGC}$  mass difference discussed in Fig. 9 must be certainly hydrogen mass produced using energy from the grid. This is certainly owing to irradiation hydrogen production being the same and not controlled for both  $H_{2p}$  cases. The high  $F_{GRD}$  rate with  $H_{2p}$  at 10 €/kg means that the HRS can be practically modelled as an electrolyzer that is always producing hydrogen with grid energy since operational expenses do not compromise profitability at any point.

In Fig. 11 the considered  $G_b$  and  $e_p$  profiles are presented in conjunction with  $P_{GRD}$ , from Equation (5) for  $H_{2p}$  at 2 €/kg. From these results, we can confirm that the MPC has charged the battery during the night and discharged it during daylight, behaviour that can be now correlated to off-peak and peak time bands in  $e_p$ . In a similar manner, the optimal total grid consumption,  $P_{GRD}$ , is greatly lower during peak  $e_p$  values.  $P_{GRD}$  having negative values means that energy injection/selling to the utility grid has been considered the optimal strategy in some cases. It is also important to note that there are complete days with close to no direct beam direct beam irradiance,  $G_b$ , so green hydrogen production is not possible. This can be confirmed with  $F_{GRD}$  being set at high rates during those time periods.

Fig. 11 results show a more comprehensive behaviour than the evolution of the states, in which it can be seen how the MPC has intelligently optimized consumption in terms of the predicted data.

Finally, it is important to note that for a  $H_{2p}$  at 10 €/kg, the  $H_p$ , in the one to seven-day range, has not shown clear trends, as Fig. 6 presents. This can be explained since the HRS optimal behaviour for this setting is to service mass to MEGC as fast as possible if it is feasible, as discussed in Fig. 10. Hence, prediction data longer than one day has shown no alteration in the final  $J_{PRS}$  nor the Economic Balance. The insignificant differences can be due to the rounding error of the solver.

In the case of the rule-based control method, results for  $H_{2p}$  at 2 €/kg show a final economic result of 4034 € in losses and for  $H_{2p}$  at 10 €/kg, 14,872 € in profits are achieved. All the configurations of the MPC tested show a significant advantage in economic performance in front of the rule-based control. This advantage is clearly shown for every weighting configuration and prediction horizon in Fig. 12. All the results mentioned in this paragraph are the result of the same levelization applied in Fig. 6.

### Conclusions

This work has introduced a general HRS layout, its modelling, MPC formulation, and performance analysis. Therefore, this study creates a framework from which each of the four mentioned topics can be exploited in future work. Furthermore, a case study is specified and analysed in detail to show the capabilities of the presented model and associated MPC.

The HRS layout and model presented in this work offers high flexibility in its operation since it presents multiple buffer states, active elements, parameters, and disturbances that directly affect performance based on a real plant that is set to be built in Zaragoza, Spain.

The MPC presented in this work has correctly serviced all vehicles' demand and has feasibly controlled all 210 simulations of one-month length, showing the potential that a predictive optimal control can provide to the future of HRS systems. The weighting of the presented multi-objective function has been studied, as well as the prediction horizon length and the hydrogen selling price effects.

The results analysis provided in this work has shown some dependencies and tendencies such as a significant difference between a prediction horizon of one day or seven days, the former showing an average 57% increase in profits for all weighting configurations. MPC has been able to achieve economic profits with a low hydrogen price compared to the losses of the rule-based control method.

Important conclusions have been argued such as the battery capacity needs to be higher to significantly affect predictive control strategies performance. Additionally, how predictive control comes to be really resolute with a low hydrogen selling price.

The main contribution of this work is that it presents a flexible framework for HRS systems design and optimal online control. As future work, the presented linear model should evolve into a hybrid model, where unit-commitment models can be introduced and some assumptions can be removed. Moreover, the layout flexibility and component sizing could be tested with optimization-based solutions, taking a techno-economic analysis approach.

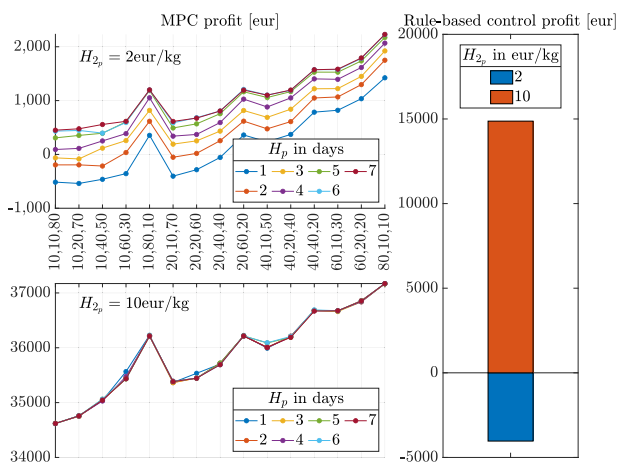


**Fig. 12 – Levelized final profit of the month of simulation in terms of the control strategy,  $H_{2p}$ , and, in the case of MPC,  $H_p$  and weight configuration as x-axis, in  $Q_p, Q_r, Q_s$  [%] format.**

The MPC could be improved if uncertainty in states or disturbances prediction is considered since uncertainty will most certainly exist in a real-life application and can heavily affect either feasibility or performance. Hence, Stochastic MPC would be the next step. In addition, a time-band variable scaling of  $J_p$  could better address  $Q_p$  significance since all disturbances involved in  $J_p$  can be short-term predicted with respectable accuracy. Additionally, weighting configuration could be variable. Finally, based on degradation effects or other reasons, softening weights could be a result of a grounded scaling of each individual softening desired levels or even some constraints in control inputs variation could be introduced based on actuator data.

### Declaration of competing interest

The authors declare that they have no known competing financial interests or personal relationships that could have appeared to influence the work reported in this paper.

### Acknowledgements

This research has been developed within the CSIC Interdisciplinary Thematic Platform (PTI+) Transición Energética Sostenible+ (PTI-TRANSENER+)[TRE2103000] as part of the CSIC program for the Spanish Recovery, Transformation and Resilience Plan funded by the Recovery and Resilience Facility of the European Union, established by the Regulation (EU) 2020/2094; project MASHED [TED2021-129927B–I00] funded by MCIN/AEI/10.13039/501100011033 and by the “European Union NextGenerationEU/PRTR”; and the project MAFALDA [PID2021-126001OB-C31] funded by MCIN/AEI/10.13039/501100011033 and by “ERDF A way of making Europe”.

### REFERENCES

- [1] Agency IIE. Global hydrogen review 2022. 2022. URL, [www.iea.org/t&c/](http://www.iea.org/t&c/).
- [2] Apostolou D, Xydis G. A literature review on hydrogen refuelling stations and infrastructure. current status and future prospects. 10 2019. <https://doi.org/10.1016/j.rser.2019.109292>.
- [3] Repsol. Nace el corredor del hidrógeno del ebro, referente para desarrollar esta energía renovable. URL, <https://www.repsol.com/es/sala-prensa/notas-prensa/2022/nace-el-corredor-del-hidrogeno-del-ebro-referente-para-desarrollar-esta-energia-renovable/index.cshtml>.
- [4] HidrogenoVerde. Presentación oficial del corredor del hidrógeno del ebro. URL, <https://hidrogeno-verde.es/nace-corredor-del-hidrogeno-del-ebro/>.
- [5] Kurtz SSJ, Bradley TH. Review of transportation hydrogen infrastructure performance and reliability. 5 2019. <https://doi.org/10.1016/j.ijhydene.2019.03.027>.
- [6] Pescbika W. Operating characteristics of a lh2-fuelled automotive vehicle and of a semi-automatic lh2-refuelling station. 1982.
- [7] Bhan V. Optimization of hydrogen filling station. 2006.
- [8] Deshmukh S, Baghzouz Y, Boehm RF. Design of grid connected-pv system for a hydrogen refueling station. 2007. p. 171–5. <https://doi.org/10.1115/ISEC2006-99151>.
- [9] Campbell MR. Monitoring and modeling the performance of a solar powered hydrogen filling station hydrogen filling station. 2009. <https://doi.org/10.25669/67hd-8zdv>. URL, <https://digitalscholarship.unlv.edu/rtds>.
- [10] He C, Sun H, Xu Y, Lv S. Hydrogen refueling station siting of expressway based on the optimization of hydrogen life cycle cost. Int J Hydrogen Energy 2017;42:16313–24. <https://doi.org/10.1016/j.ijhydene.2017.05.073>.
- [11] Sun H, He C, Wang H, Zhang Y, Lv S, Xu Y. Hydrogen station siting optimization based on multi-source hydrogen supply and life cycle cost. Int J Hydrogen Energy 2017;42:23952–65. <https://doi.org/10.1016/j.ijhydene.2017.07.191>.
- [12] Zhe Wang DW, Zhao F, Han F, Ji Y, Cai W. Hydrogen refueling stations and carbon emission reduction of coastal expressways: a deployment model and multi-scenario analysis. J Mar Sci Eng 2022;10:992. <https://doi.org/10.3390/jmse10070992>.
- [13] Wang Y, Kazemi M, Nojavan S, Jermisittiparsert K. Robust design of off-grid solar-powered charging station for hydrogen and electric vehicles via robust optimization approach. Int J Hydrogen Energy 2020;45:18995–9006. <https://doi.org/10.1016/j.ijhydene.2020.05.098>.
- [14] Dadkhah A, Bozalakov D, Kooning JDD, Vandeveld L. On the optimal planning of a hydrogen refuelling station participating in the electricity and balancing markets. Int J Hydrogen Energy 2021;46:1488–500. <https://doi.org/10.1016/j.ijhydene.2020.10.130>.
- [15] Sun J, Peng Y, Lu D, Chen X, Xu W, Weng L, Wu J. Optimized configuration and operating plan for hydrogen refueling station with on-site electrolytic production. Energies 4 2022;15. <https://doi.org/10.3390/en15072348>.
- [16] Luo H, Xiao J, Bénard P, Chahine R, Yang T. Multi-objective optimization of cascade storage system in hydrogen refuelling station for minimum cooling energy and maximum state of charge. Int J Hydrogen Energy 2022;47:10963–75. <https://doi.org/10.1016/j.ijhydene.2022.01.059>.
- [17] Barhoumi EM, Okonkwo PC, Farhani S, Belgacem IB, Zghaibeh M, Mansir IB, Bacha F. Techno-economic analysis of photovoltaic-hydrogen refueling station case study: a transport company tunis-Tunisia. Int J Hydrogen Energy 2022;47:24523–32. <https://doi.org/10.1016/j.ijhydene.2021.10.111>.
- [18] Barhoumi EM, Okonkwo PC, Belgacem IB, Zghaibeh M, Tlili I. Optimal sizing of photovoltaic systems based green hydrogen refueling stations case study Oman. Int J Hydrogen Energy 2022;47:31964–73. <https://doi.org/10.1016/j.ijhydene.2022.07.140>.
- [19] Aki H, Sugimoto I, Sugai T, Toda M, Kobayashi M, Ishida M. Optimal operation of a photovoltaic generation-powered hydrogen production system at a hydrogen refueling station. Int J Hydrogen Energy 2018;43:14892–904. <https://doi.org/10.1016/j.ijhydene.2018.06.077>.
- [20] Zhao L, Brouwer J. Dynamic operation and feasibility study of a self-sustainable hydrogen fueling station using renewable energy sources. Int J Hydrogen Energy 2015;40:3822–37. <https://doi.org/10.1016/j.ijhydene.2015.01.044>.
- [21] Xu X, Hu W, Cao D, Huang Q, Liu W, Jacobson MZ, Chen Z. Optimal operational strategy for an offgrid hybrid hydrogen/electricity refueling station powered by solar photovoltaics. J Power Sources 3 2020;451. <https://doi.org/10.1016/j.jpowsour.2020.227810>.
- [22] Dispenza G, Sergi F, Napoli G, Randazzo N, Novo SD, Micari S, Antonucci V, Andaloro L. Development of a solar powered hydrogen fueling station in smart cities applications. Int J Hydrogen Energy 2017;42:27884–93. <https://doi.org/10.1016/j.ijhydene.2017.07.047>.

- [23] Akbari-Dibavar A, Tabar VS, Zadeh SG, Nourollahi R. Two-stage robust energy management of a hybrid charging station integrated with the photovoltaic system. *Int J Hydrogen Energy* 2021;46:12701–14. <https://doi.org/10.1016/j.ijhydene.2021.01.127>.
- [24] Carr S, Zhang F, Liu F, Du Z, Maddy J. Optimal operation of a hydrogen refuelling station combined with wind power in the electricity market. *Int J Hydrogen Energy* 2016;41:21057–66. <https://doi.org/10.1016/j.ijhydene.2016.09.073>.
- [25] Okonkwo PC, Mansir IB, Barhoumi EM, Emori W, Radwan AB, Shakoor RA, Uzoma PC, Pugalenth MR. Utilization of renewable hybrid energy for refueling station in al-kharj, Saudi Arabia. *Int J Hydrogen Energy* 2022;47:22273–84. <https://doi.org/10.1016/j.ijhydene.2022.05.040>.
- [26] Mehrjerdi H. Off-grid solar powered charging station for electric and hydrogen vehicles including fuel cell and hydrogen storage. *Int J Hydrogen Energy* 2019;44:11574–83. <https://doi.org/10.1016/j.ijhydene.2019.03.158>.
- [27] Heere D. *Modelling and optimization of a hydrogen refuelling station based on ch2p technology delivering decentralized hydrogen and electricity for mobility by daniel heere*. 2019.
- [28] Xiao L, Chen J, Wu Y, Zhang W, Ye J, Shao S, Xie J. Effects of pressure levels in three-cascade storage system on the overall energy consumption in the hydrogen refueling station. *Int J Hydrogen Energy* 2021;46:31334–45. <https://doi.org/10.1016/j.ijhydene.2021.07.007>.
- [29] Çiçek A. Optimal operation of an all-in-one ev station with photovoltaic system including charging, battery swapping and hydrogen refueling. *Int J Hydrogen Energy* 2022;9. <https://doi.org/10.1016/j.ijhydene.2022.07.171>.
- [30] Wu X, Zhao W, Li H, Liu B, Zhang Z, Wang X. Multi-stage stochastic programming based offering strategy for hydrogen fueling station in joint energy, reserve markets. *Renew Energy* 2021;180:605–15. <https://doi.org/10.1016/j.renene.2021.08.076>.
- [31] Aki H, Sugimoto I, Toda M, Sugai T, Kobayashi M, Fujisawa A, Taniguchi Y, Ishida M. *Electrolysis system operation strategies for a hydrogen refueling station using renewable energy sources*. 2018.
- [32] Panah PG, Bornapour M, Hemmati R, Guerrero JM. Charging station stochastic programming for hydrogen/battery electric buses using multi-criteria crow search algorithm. *Renew Sustain Energy Rev* 2021;144. <https://doi.org/10.1016/j.rser.2021.111046>.
- [33] Zhu L, He J, He L, Huang W, Wang Y, Liu Z. Optimal operation strategy of pv-charging-hydrogenation composite energy station considering demand response. *Energies* 2022;15:5915. <https://doi.org/10.3390/en15165915>.
- [34] Pang Y, Pan L, Zhang J, Chen J, Dong Y, Sun H. Integrated sizing and scheduling of an off-grid integrated energy system for an isolated renewable energy hydrogen refueling station. *Appl Energy* 10 2022;323. <https://doi.org/10.1016/j.apenergy.2022.119573>.
- [35] Wang M, Dong X, Zhai Y. Optimal configuration of the integrated charging station for pv and hydrogen storage. *Energies* 11 2021;14. <https://doi.org/10.3390/en14217087>.
- [36] Rothuizen E, Mérida W, Rokni M, Wistoft-Ibsen M. Optimization of hydrogen vehicle refueling via dynamic simulation. *Int J Hydrogen Energy* 2013;38:4221–31. <https://doi.org/10.1016/j.ijhydene.2013.01.161>.
- [37] Jrc photovoltaic geographical information system (pvgis) - european commission. URL, [https://re.jrc.ec.europa.eu/pvg\\_tools/en/](https://re.jrc.ec.europa.eu/pvg_tools/en/).
- [38] Pvpcc | esios electricidad. URL, <https://www.esios.ree.es/es/pvpcc>.
- [39] Luna J, Ocampo-Martinez C, Serra M. Nonlinear predictive control for the concentrations profile regulation in a pem fuel cell anode gas channel. *Institute of Electrical and Electronics Engineers Inc.*; 2014. p. 1807–12. <https://doi.org/10.1109/ECC.2014.6862495>.
- [40] Löfberg J. *Yalmip : a toolbox for modeling and optimization in matlab*. In: *Proceedings of the CACSD Conference*. Taiwan: Taipei; 2004.
- [41] Gurobi optimization, LLC, Gurobi optimizer reference manual. URL. 2022. <https://www.gurobi.com>.